FULL PAPER

Possible fluid discharge associated with faults observed by a high-resolution dense-2D seismic reflection survey in Uchiura Bay off Numazu, Japan

Tetsuro Tsuru[1*] , Jin-Oh Park[2], Kazuo Amakasu[1], Tetsuo No[3], Kohsaku Arai[4], Takahiko Inoue[4], Seishiro Furuyama[1], Keiichi Uchida[1] and Yasuyuki Nakamura[3]

Abstract

Although fluid behavior along faults has often been associated with earthquakes and hydrocarbon accumulation, few observations of active, ongoing fluid discharge along the faults exist. We conducted a dense-2D multi-channel seismic (MCS) reflection survey in Uchiura Bay off Numazu, Japan, in 2018 to obtain a high-resolution image of active faults. As a result, active faults cutting the seafloor and possibly active faults cutting reflections immediately below the seafloor have been clearly imaged on MCS profiles. The spatial variation in their displacement on the seafloor has also been quantified. The seafloor displacement of the most obvious active fault, Fault A, changes by more than 2 m within a short horizontal distance of 50 m. On one of the MCS profiles, an enigmatic wavefield (EWF) is observed within the water column above the seafloor near the faults. From careful observations of the raw field data and shot records, the EWF shows three patterns that suggest fluid flow. Based on a velocity analysis of the seawater, the velocity of the EWF zone was somewhat higher than that of its surroundings. Because the seawater velocity is a function of temperature and salinity at the same depth, the effect of temperature is generally greater than that of salinity, so that the higher velocity would suggest a higher temperature. If temperature of the fluid flow is higher than that of its surroundings, the fluid would rise with its buoyancy and spread out along the sea surface. This scenario could well explain the three EWF patterns. From the appearance and non-appearance of the most obvious EWF on adjacent seismic lines, some fluid discharge might have been occurring intermittently from the seafloor near the faults in Uchiura Bay.

Keywords: Fluid discharge, Active fault, High-resolution multichannel seismic survey, Seismic attenuation, Uchiura Bay

Introduction

The existence of fluid flow along faults is reported by scientific drilling (e.g., ODP Leg 110 Scientific Party 1987) and suggested by multi-channel seismic (MCS) surveys (e.g., Shipley et al. 1994; Park et al. 2002). Gray et al. (2019) suggested fluid flow from low-velocity faults by a high-resolution 2D velocity model from the full-waveform inversion of MCS data. These studies suggest possible continuous fluid flows along large fault shear zones, such as a plate boundary décollement and splay fault detached from the plate boundary. In addition to continuous flows, episodic flows are suggested by some seafloor geophysical observations after the 2011 Tohoku earthquake (Sano et al. 2014; Tsuji et al. 2013). Sano et al. (2014) identified the rapid movement of fluids from the

*Correspondence: ttsuru0@kaiyodai.ac.jp
[1] Department of Marine Resources and Energy, Tokyo University of Marine Science and Technology, 4-5-7 Konan, Minato-ku, Tokyo 108-8477, Japan
Full list of author information is available at the end of the article

Tsuru *et al. Earth, Planets and Space* (2020) 72:121

Page 2 of 15

mantle to the seafloor along the plate interface, based on helium anomalies in seawater near the rupture zone one month after the earthquake. Tsuji et al. (2013) observed anomalously high heat flow on the seafloor at a normal fault 5 months after the earthquake. Both observations suggest rapid fluid flows via faults during earthquakes. Except for a few seismic imaging studies (e.g., Chen et al. 2017), examples of visually imaged ongoing fluid discharges from the seafloor along faults are rare. We conducted a high-resolution dense-2D MCS reflection survey in Uchiura Bay off Numazu, Japan, in 2018 to investigate active faults and fluid flows along faults near the seafloor.
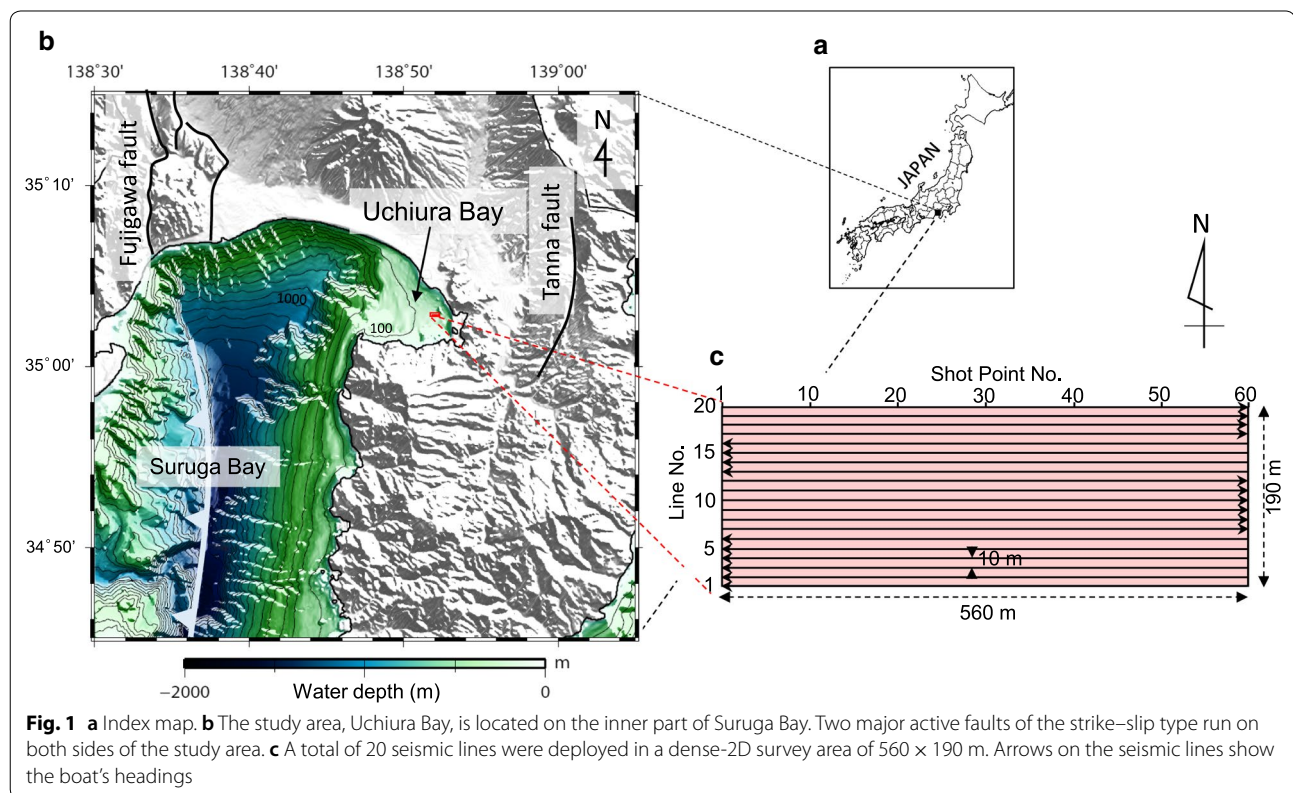
Uchiura Bay is located in the inner part of the Suruga Bay (Fig. 1), where the Philippine Sea Plate is subducting beneath the Eurasia Plate. It exhibits the widest continental shelf (ca. 10 km) in Suruga Bay with a gentle dip toward the west (Misawa 1990). Uchiura Bay can be classified as a tectonically active region, as it is situated between two major active faults of the left-lateral strike–slip type, Fujikawa fault and Tanna fault, which were activated in 1854 (Tsuneishi and Shiosaka 1981; Nishimura et al. 1986) and 1930 (Tanna Fault Trenching Research Group 1983), respectively. The strikes of these faults are chiefly N–S and partly NE–SW or NW–SE. Furthermore,

an active fault with a possible N–S strike is reported in Uchiura Bay in a seismic study (Sato 2014). Here, we report on some active and potentially active faults discovered by the MCS survey. In this paper, we argue that the EWF may be related to fluid flow associated with these newly mapped faults or fault shear zones.

Seismic reflection survey and data processing

On August 7, 2018, a high-resolution dense-2D MCS survey was conducted in Uchiura Bay (Fig. 1a, b) by chartering the *S/B Daini-Ikoimaru* of Oki Seatec Co., Ltd. Twenty lines of MCS data were collected in an E-W direction in a survey area of 560×190 m (Fig. 1c). An underwater speaker was used as a non-explosive (non-impulsive) seismic source (Tsuru et al. 2019), which has almost flat frequency response over 100–10,000 Hz. The shot intervals were 6 s, corresponding to a shot point interval of about 6 m at a boat speed of 2 kn in case of no water current, which was the standard boat speed in this survey.

The Navlog made by Marimex Japan K.K. was used as the navigation system in the survey. The X–Y coordinates of shots and receivers were calculated from the boat positions provided by this system based on the differential GPS, assuming a straight streamer cable without cable

Fig. 1 **a** Index map. **b** The study area, Uchiura Bay, is located on the inner part of Suruga Bay. Two major active faults of the strike–slip type run on both sides of the study area. **c** A total of 20 seismic lines were deployed in a dense-2D survey area of 560 × 190 m. Arrows on the seismic lines show the boat's headings

Tsuru *et al. Earth, Planets and Space*   (2020) 72:121

Page 3 of 15

feathering (the angle between the actual cable position and the track line of the survey boat).

For the source waveform, we created a pseudorandom wave of 5 s with the Mersenne Twister (Matsumoto and Nishimura 1998) function in the numerical analysis software MATLAB developed by the MathWorks, Inc. The Mersenne Twister is the most commonly used pseudorandom number generator developed by using the m-sequence.

The recording was done using a 16-channel streamer cable with a group spacing of 3.125 m; the sampling interval was 0.5 ms. The raw field data collected by the observation system using a non-explosive source do not resemble a conventional seismic record by an explosive seismic source, since it consists of a composite of overlapping 5-s reflections from each reflector. This is similar to onshore seismic field recording with a Vibroseis system. Cross-correlation processing is commonly applied to convert the non-explosive field records into conventional impulsive seismic records (e.g., Yilmaz and Doherty 1987). The cross-correlation of each trace of the raw field record with the transmitted source wave effectively results in pulse compression of the reflected wave trains, producing a conventional shot record. This data processing procedure is the same as that used in onshore Vibroseis surveys (Yilmaz and Doherty 1987).

Cross-correlation, normal-moveout (NMO) correction, and stacking with the pre-stack profiling method (Nagumo 2000) were followed by a band-pass filter. The pre-stack profiling method stacks the NMO-corrected traces of each shot record assuming a horizontally layered media. Although the horizontal resolution of this method is low, it can offer a higher signal-to-noise ratio when the common depth point (CDP) stacking fold is low. In this survey, the CDP stack fold was 4, compared with 16 for the pre-stack profiling method. The pre-stack profiling method was also chosen due to CDP stacking fold inconsistencies in this survey due to shooting at a constant time interval (not at constant distance).

However, the pre-stack profiling sometimes caused inconsistencies in the number of stacked-traces per line due to the inconsistency of boat's speed. Therefore, we divided each line into 60 cells and then put stacked-traces in their corresponding cells. When there is no trace put in a cell, a new trace is synthesized by a spatial interpolation function (resample) of MATLAB. Conversely, when multiple traces are present in a cell, the exceeded traces are decimated. As shown in Additional file 1, 10–17% of empty cells were interpolated in lines 1–5. No empty cells interpolated in the other lines are present because of improved skills in low-speed (2 kn) boat control during the survey. Consequently, a small-scale 3D cube was formed with these regular 60 traces per line from the

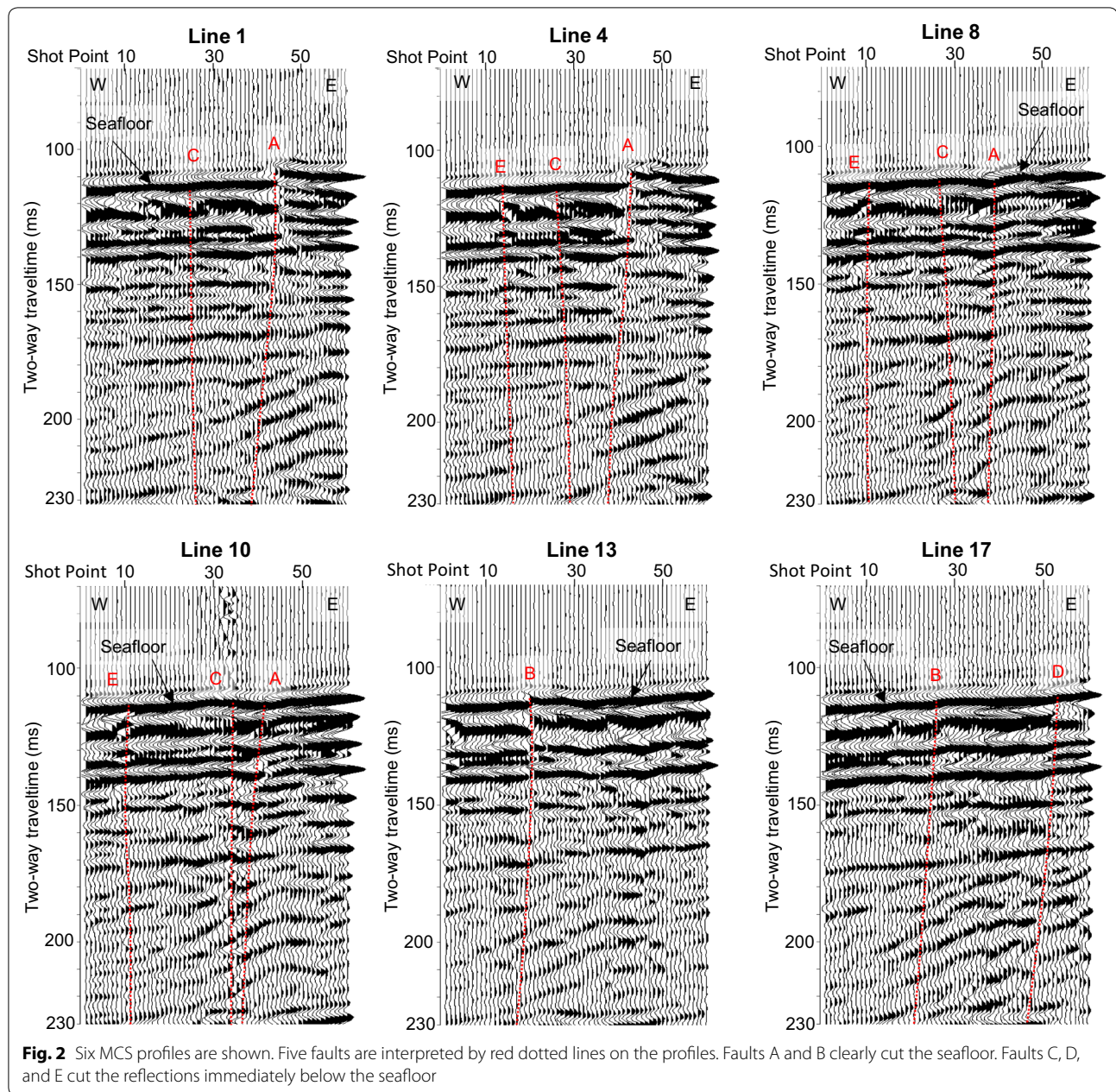dense-2D dataset. Examples of the resulting MCS profiles are shown in Fig. 2.

In addition to the conventional seismic data processing mentioned above, seismic attenuation profiling (SAP) (Additional file 2) was applied for fault interpretation. Time slices from the 3D MCS cube are generally used for fault trend detection; however, specifying faults where clear seismic reflections are not observed is difficult (Tsuru et al. 2018). However, SAP uses spatial variation in frequency content rather than amplitude, meaning that this method does not require clear continuous reflections with a predominant amplitude. Tsuru et al. (2017) successfully imaged a fractured zone as a high-attenuation anomaly in a volcanic area. In the present study, a Q slice from SAP was used for fault trend analysis, where no clear continuous reflections were visible. Here, the Q slice means a horizontal slice from a 3D cube of quality factor Q computed by SAP.

Results

Fault interpretation

Five faults were successfully imaged on the MCS profiles (Fig. 2). Among them, two faults (A and B) show clear displacement at the seafloor and are interpreted as active faults due to the offset of the seafloor reflections. Here we look at fault displacement on the seafloor from the south to the north in the survey area. Fault A exhibits a large vertical displacement of 2.1–3.2 ms in two-way travel time (1.6–2.4 m for a velocity of 1500 m/s) at the seafloor on lines 1–6 (lines 1 and 4 shown in Fig. 2; Additional file 3) in the survey area. The vertical displacement unexpectedly decreases up to 0.1–1.0 ms in two-way travel time (0.075–0.75 m for a velocity of 1500 m/s) at the seafloor on lines 7–10 (lines 8 and 10 shown in Fig. 2; Additional file 3). The vertical displacement at the seafloor as well as below is no longer visible north of line 10 (lines 13 and 17 shown in Fig. 2; Additional file 3). This spatial variation in vertical displacement on the seafloor exceeds 2 m within a short horizontal distance of 50 m. Fault B has a relatively small but clear vertical displacement at the seafloor on lines 13–20 (lines 13 and 17 in Fig. 2; Additional file 3). Also, three further faults (C, D, and E) can be identified by offsets of reflections immediately below the seafloor. However, identifying their vertical displacements at the seafloor is somewhat challenging. Therefore, we interpreted those three faults as potentially active faults, in consideration of the offsets of reflections immediately below the seafloor.

The fault trend was analyzed on the MCS profiles and mapped onto time slices in Fig. 3a, b. In Fig. 3a, the resulting fault strikes are consistent with the sharp changes in reflection amplitude on the time slice at 140 ms in two-way travel time. In Fig. 3b, the spatial

Tsuru *et al. Earth, Planets and Space* (2020) 72:121

Page 4 of 15

Fig. 2 Six MCS profiles are shown. Five faults are interpreted by red dotted lines on the profiles. Faults A and B clearly cut the seafloor. Faults C, D, and E cut the reflections immediately below the seafloor

variation in amplitude is a little vague on the time slice at 220 ms in two-way travel time, because continuous reflections with predominant amplitudes are invisible on the MCS profiles at this travel time. Therefore, we also show a Q slice at 220 ms from the SAP analysis in Fig. 3c. The fault locations appear to be consistent with the high-attenuation anomalies (red-to-yellow colors in Fig. 3c). Fault C is clear on the time slices of 120–180 ms in two-way travel time (time slice of 140 ms in Fig. 3a; Additional file 4) and can be identified on the Q slices deeper than 200 ms (Q slice of 220 ms in Fig. 3c; Additional file 5).

Thus, combining both slices allow easier the interpretation of fault trend. As shown in Fig. 3, the faults exhibit three clear strikes: N–S, NE–SW (or NNE–SSW), and NW–SE (or NNW–SSE).

Displacement–length analysis of the faults observed in the survey was conducted based on the fault interpretation on each MCS profile as shown in Fig. 4. Regular accumulations of displacement by fault slips are not clearly seen on every fault. Because horizontal components of the fault displacements are not identified on the present seismic data, we plotted their vertical
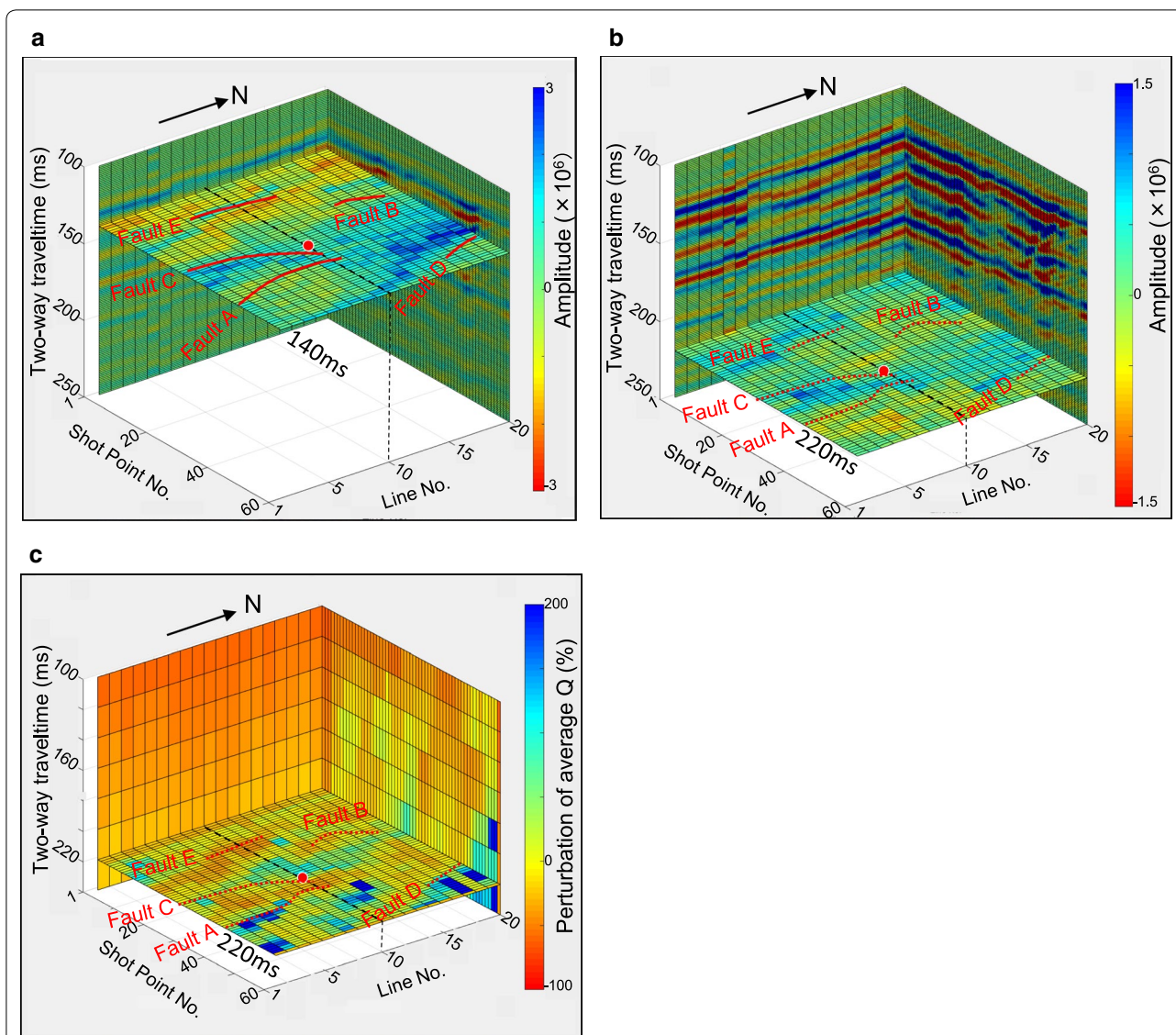
Tsuru *et al. Earth, Planets and Space*   (2020) 72:121

Page 5 of 15

Fig. 3 **a** Time slice of 140 ms in two-way travel time. The strikes of the specified faults are consistent with the spatial variation in amplitude. A red circle marks the location of the most obvious EWF. **b** Time slice at 220 ms. The fault strike seems to be consistent with the spatial variation in amplitude but is somewhat difficult to see. **c** Q slice at 220 ms. The fault strikes seem to be consistent with a high-attenuation anomaly (red-to-yellow colors), especially between Faults A and C

displacements in the displacement–length diagrams. Here, the conversion from two-way travel time to depth for the calculation of fault length was made using the constant velocity of 1500 m/s because the survey area is small, and the target depth is shallow. Regarding fault dip, every fault demonstrates an almost vertical dip (Fig. 2).

Enigmatic wavefield

An enigmatic wavefield (EWF) can be observed within the water column on the MCS profile of line 10 (Fig. 5). When observing this line, the sea state was calm, and no large vessels (causing considerable noise) approached

the survey boat. Therefore, the EWF is unlikely to be ship noises. What is the cause of the EWF, a shoal of fish, earthquake, or gases (or fluids)? The EWF is probably not a shoal of fish because of its continuous distribution, greater than 70 m, from the seafloor to the sea surface. It also cannot be an earthquake because no earthquakes occurred during the observations in and around Uchiura Bay.

To clarify the nature of the EWF that appeared on the MCS profile (stack section) of line 10, we checked whether or not the EWF can be also observed on the shot records after the cross-correlation as well as on the
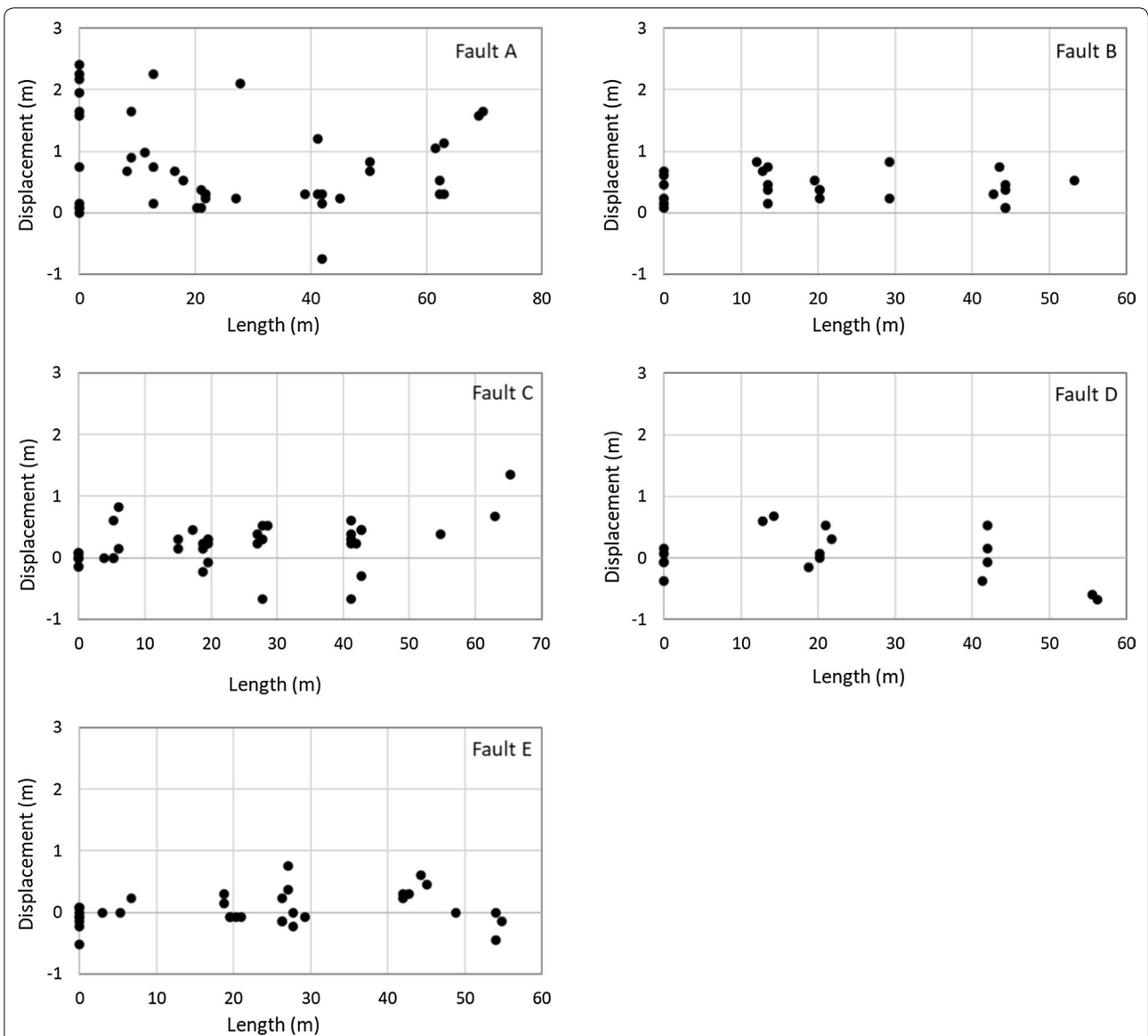
Tsuru *et al. Earth, Planets and Space*   (2020) 72:121

Page 6 of 15

Fig. 4 Displacement versus length diagrams are shown for the faults interpreted from the MCS profiles. The conversion from two-way travel time to depth to calculate the fault length was done using a constant velocity of 1500 m/s
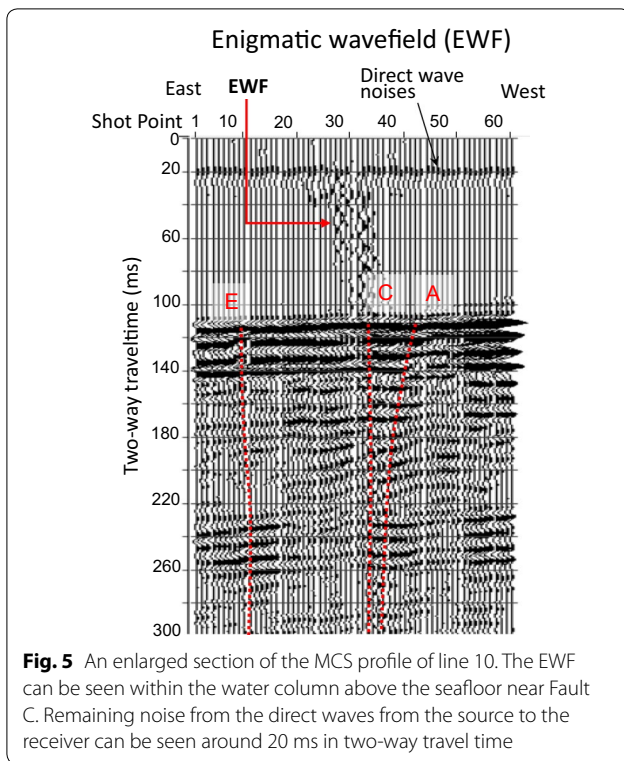
raw field data before the cross-correlation. If the EWF is seen on the shot records but not on the raw field data, the EWF should be related to some reflectors within the water column. If the EWF is also seen on the raw field data, the EWF may be related to some waves (not reflections) associated with gases (or fluids).

Therefore, we searched the EWF exhaustively in both shot records and raw field data. As a result, the EWFs were recognized on both data sets not only on line 10 (Fig. 6) but also on lines 3, 5, 7, 10, 14, 16 and 17 (Additional file 6). Among these EWFs, the most evident EWF is that of line 10, showing a noticeable difference in

rms amplitude level from its surroundings as shown in Fig. 6b.

Velocity analysis of the water column was conducted to verify whether or not the EWF was associated with gases. The velocity must be less than the sound velocity of the seawater if gases caused the EWF. As shown in Fig. 7, the velocity of the EWF zone becomes higher than that of its surroundings, showing a velocity of 1580 m/s at a maximum. This means there is a low possibility of gases being the cause of the EWF.

Here, we examine the accuracy of the velocity estimation in the study. The geometry of the receivers and

Tsuru *et al. Earth, Planets and Space*   (2020) 72:121

Page 7 of 15

Fig. 5 An enlarged section of the MCS profile of line 10. The EWF can be seen within the water column above the seafloor near Fault C. Remaining noise from the direct waves from the source to the receiver can be seen around 20 ms in two-way travel time

the source is critically important to get correct seismic velocity by NMO corrections. If the streamer cable bends, the source–receiver offsets become smaller, and a higher apparent velocity is estimated. In Uchiura Bay, the water current is generally 0.1–0.2 kn, excluding a higher current of 1–2 kn that was observed once or twice a day (informed by Mr. Takekoshi T., Oki Seatec Co., Ltd.). Therefore, no extensive feathering was generally predicted for the study area. However, because we were unable to monitor the geometry of the receivers in the survey, we calculated the velocity estimation errors from feathering. As shown in Table 1, a maximum of up to 2.7% of the velocity error is caused by feathering. However, the velocity gap between the EWF zone (1580 m/s in maximum) and the surroundings (1520 m/s) is 3.9%. Although the velocity error is notably smaller than the velocity gap, denying the possibility of feathering-oriented errors in velocity analysis would be difficult. However, considering that the direct waves from the source to the receivers are aligned straight on the shot records around the EWFs (Figs. 8, 9, 10), the influence of feathering may be limited.

Discussion
Fault interpretation
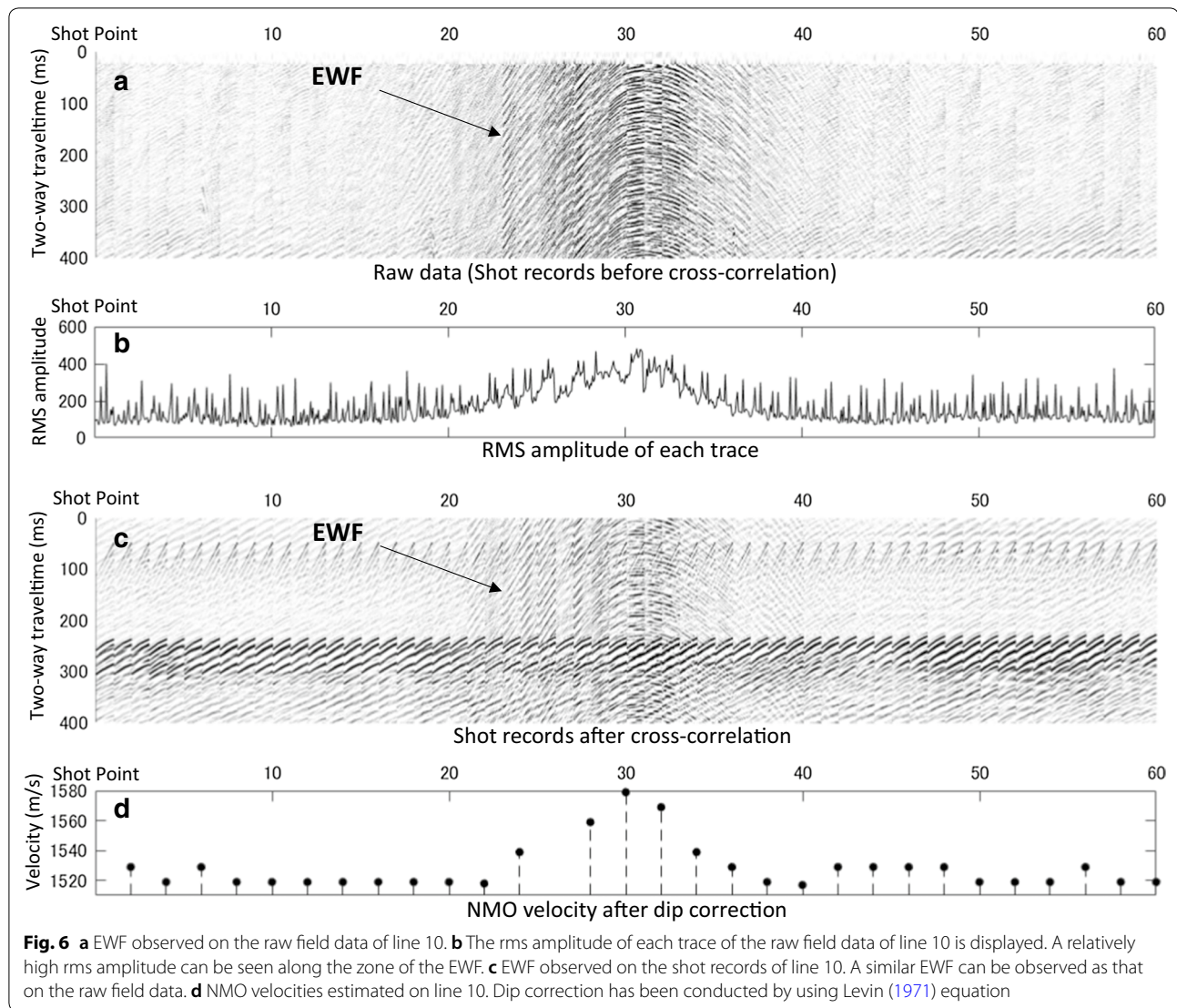The faults can be interpreted to be active or potentially active faults considering the vertical components of

the fault displacements observed at the seafloor. Given their almost vertical dips as well as no regular accumulations of their vertical displacements on the displacement–length analysis, these faults might be interpreted as strike–slip faults. Although this interpretation is still speculative because horizontal components of the fault displacements are not identified in the present study, the interpretation is consistent with the nearby major active left-lateral strike–slip faults: Fujigawa fault and Tanna fault. Hereinafter, "displacements" refer to vertical components of displacements unless otherwise noted. Fault A, which is the most obvious active fault observed in the survey, showed the largest seafloor displacement change, which exceeds 2 m within a short horizontal distance of 50 m.

Measuring the fault displacements accurately is somewhat difficult due to the relatively poor reflectivity below 150 ms in two-way travel time on the MCS profiles, as well as relatively sparse grid (9 m × 10 m) of the present dense-2D seismic data, leading to a relative decrease in the accuracy of the fault trend analysis. However, the spatial variation in amplitude on the time slice (Fig. 3a, b) appears to be consistent with the fault strikes, especially with that of Fault C. Also, the high-attenuation anomaly on the Q slice (Fig. 3c) can be seen along Fault C, which would suggest the presence of a possible fault shear zone along Fault C or between Faults A and C.

Fluid discharge
In the present study, the EWF was observed within the water column above the seafloor near the fault. As mentioned before, the EWF is unlikely to be a shoal of fish or an earthquake. Moreover, the possibility of gases being the cause of the EWF is very low based on the results of the velocity analysis of the water column. As the remaining possible causes, fluids or an artificial object (or a living thing) emitting considerably large sounds may be considered. If such an artificial object or a living thing exists in the seawater or at the seafloor, these kinds of coherent waves in the EWF could be explained. However, no such object or living thing has been reported in Uchiura Bay. Also, the higher velocity of the EWF zone (Fig. 6) cannot be explained by an artificial object or living thing.

Here, we discuss the possibility of fluid flow as the cause of the EWF. Several patterns of the EWF observed on the shot records are shown in Figs. 8, 9 and 10 to investigate the nature of the EWF. Figure 8 shows the most obvious EWF on line 10, and the EWF has stronger amplitudes than the direct waves. Figure 9 shows the EWF on line 16, which is less obvious than that of line 10 but is reasonably clear. A part of the EWF (shot point 44) show relatively high amplitudes

Fig. 6 a EWF observed on the raw field data of line 10. **b** The rms amplitude of each trace of the raw field data of line 10 is displayed. A relatively high rms amplitude can be seen along the zone of the EWF. **c** EWF observed on the shot records of line 10. A similar EWF can be observed as that on the raw field data. **d** NMO velocities estimated on line 10. Dip correction has been conducted by using Levin (1971) equation

comparable to those of line 10. Figure 10 shows the EWF on line 14, which is less obvious than those of lines 10 and 16. On the western side of shot point 46, the EWF becomes somewhat invisible due to ship noise.

More specifically, the EWF can be divided into three patterns:

Pattern 1 has the same sign of apparent phase velocity as that of a direct wave.
Pattern 2 has ~ zero apparent phase velocity (almost flat).
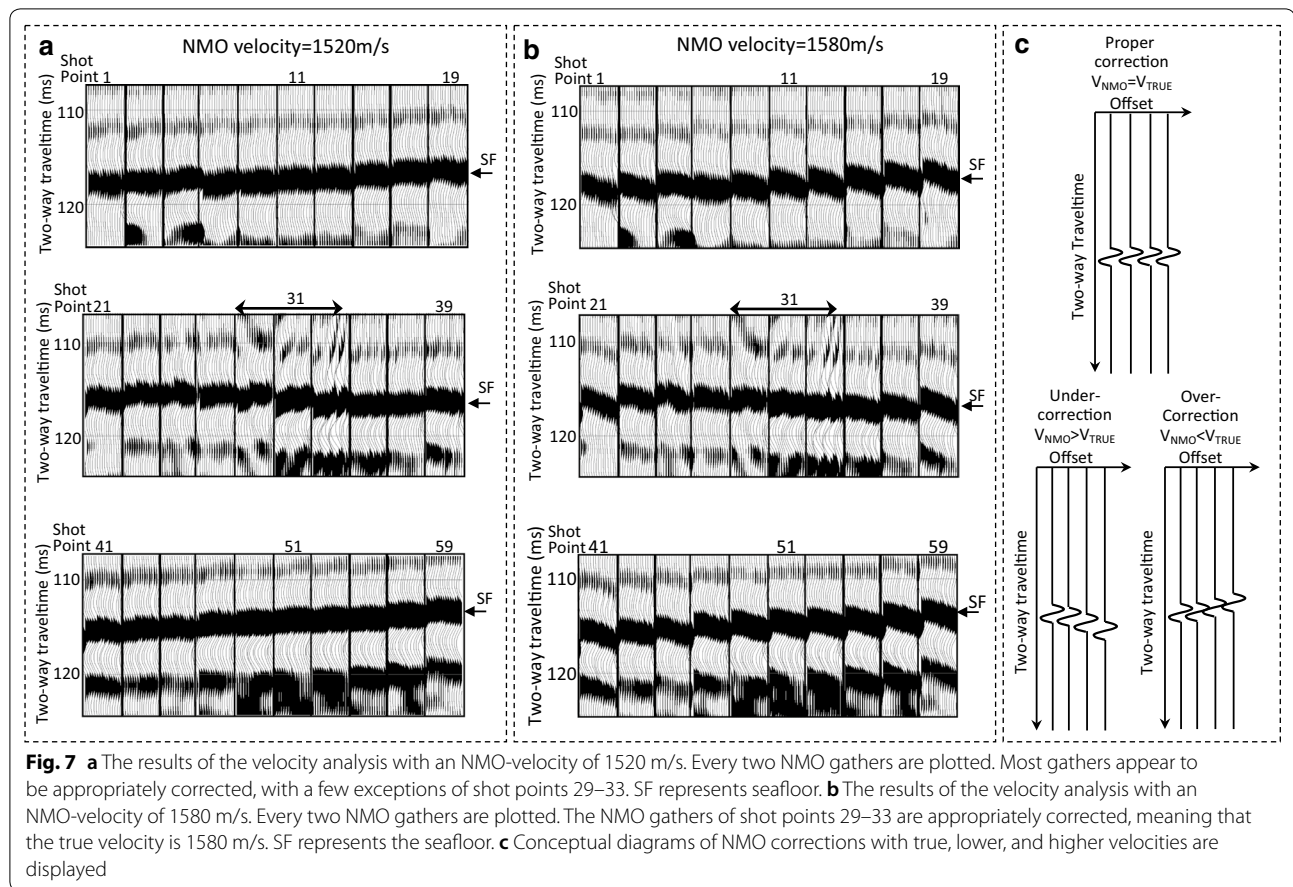Pattern 3 has the opposite sign of apparent phase velocity to that of a direct wave.

If the EWF is caused by fluid flow, these patterns on line 10 can be explained as follows:

Pattern 1 is a wavefield observed when the fluid flow apparently comes into the streamer cable from its near-offset side.
Pattern 2 is a wavefield observed when the fluid flow upwells in the water below the streamer cable.
Pattern 3 is a wavefield observed when the fluid flow apparently comes into the streamer cable from its far-offset side.

Figure 11 shows a conceptual diagram of the EWF on line 10, which shows that the three patterns of the EWF

Tsuru *et al. Earth, Planets and Space*   (2020) 72:121

Page 9 of 15

Fig. 7 a The results of the velocity analysis with an NMO-velocity of 1520 m/s. Every two NMO gathers are plotted. Most gathers appear to be appropriately corrected, with a few exceptions of shot points 29–33. SF represents seafloor. **b** The results of the velocity analysis with an NMO-velocity of 1580 m/s. Every two NMO gathers are plotted. The NMO gathers of shot points 29–33 are appropriately corrected, meaning that the true velocity is 1580 m/s. SF represents the seafloor. **c** Conceptual diagrams of NMO corrections with true, lower, and higher velocities are displayed

can be observed depending on boat positions against an upwelling fluid.

Figure 12 shows an additional conceptual diagram to explain the relatively less obvious EWFs on lines 14 (Fig. 10) and 16 (Fig. 9). The EWF patterns on lines 14 and 16 may be observed in a downwelling zone and an upwelling zone, respectively. Here, the downwelling and upwelling near the sea surface are known as the Langmuir circulations, which are wind-induced water movements with helical vortices (Langmuir, 1938).

According to the results of the velocity analysis, the seawater velocity of the EWF zone (1580 m/s maximum) is higher than that of its surroundings (1520 m/s). Seawater velocity is a function of temperature, salinity, and depth (pressure). In the present study, the depth factor can be ignored because we compare the seawater velocity laterally. According to a model for seawater velocity by using the Mackenzie (1981) equation (Additional file 7), temperatures equivalent to the velocity of 1520 m/s is 19 ℃ to 20 ℃ for a salinity range of 34‰ to 35‰. The temperature of 19 ℃ to 20 ℃ is consistent with the average temperature in Uchiura Bay, which was observed in

an environment study (Kutsuwada et al. 2007). The velocity of 1580 m/s exceeds the applicable range (≦ 30 ℃) in any equation for seawater velocity modeling. Because the effect of salinity is generally smaller than that of temperature, the higher velocity may suggest a higher temperature.

If the fluid exhibits a higher temperature than its surroundings, the fluid will rise because of its buoyancy. If the fluid rises toward the sea surface, it should be spread out along the sea surface as shown in Fig. 11a, which supports the observation of the three EWF patterns. Although the fluid flow as the cause of the EWF is still speculative because of a lack of firm evidence, such as direct measurement of temperature or sampling of high-temperature fluid; however, our observations suggest a possible fluid flow with higher temperatures within the water column.
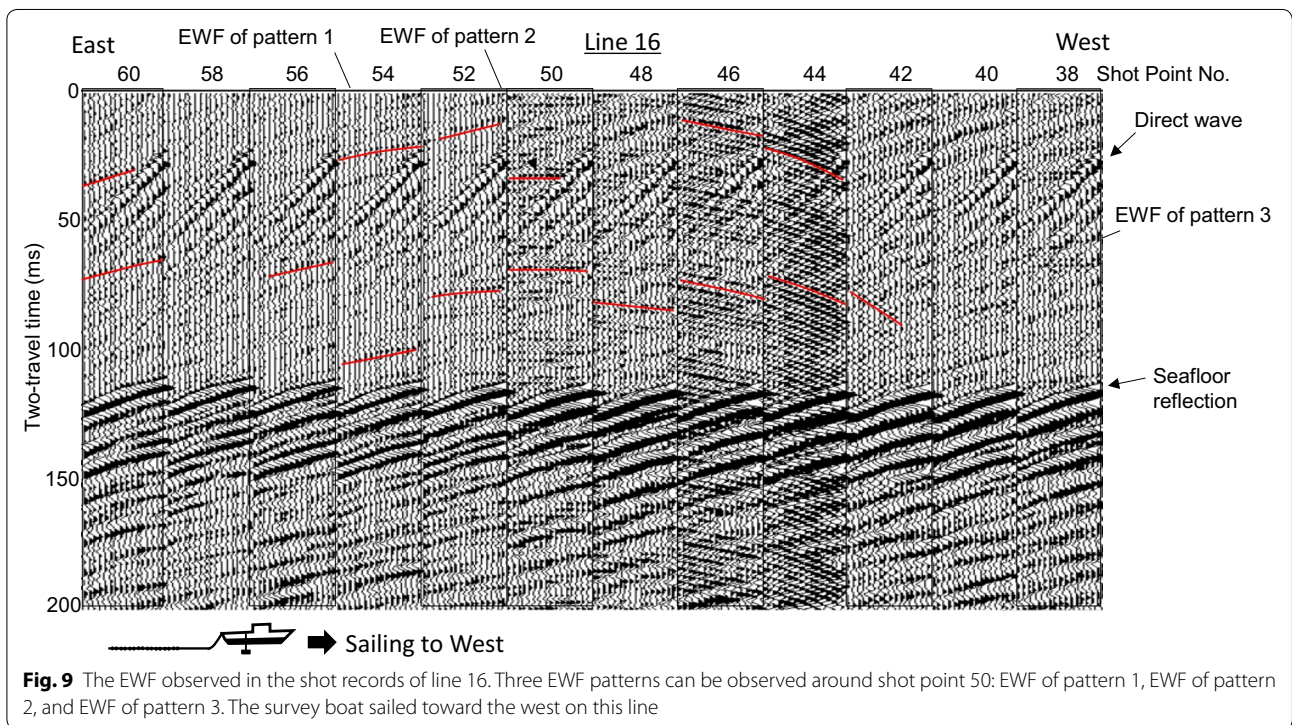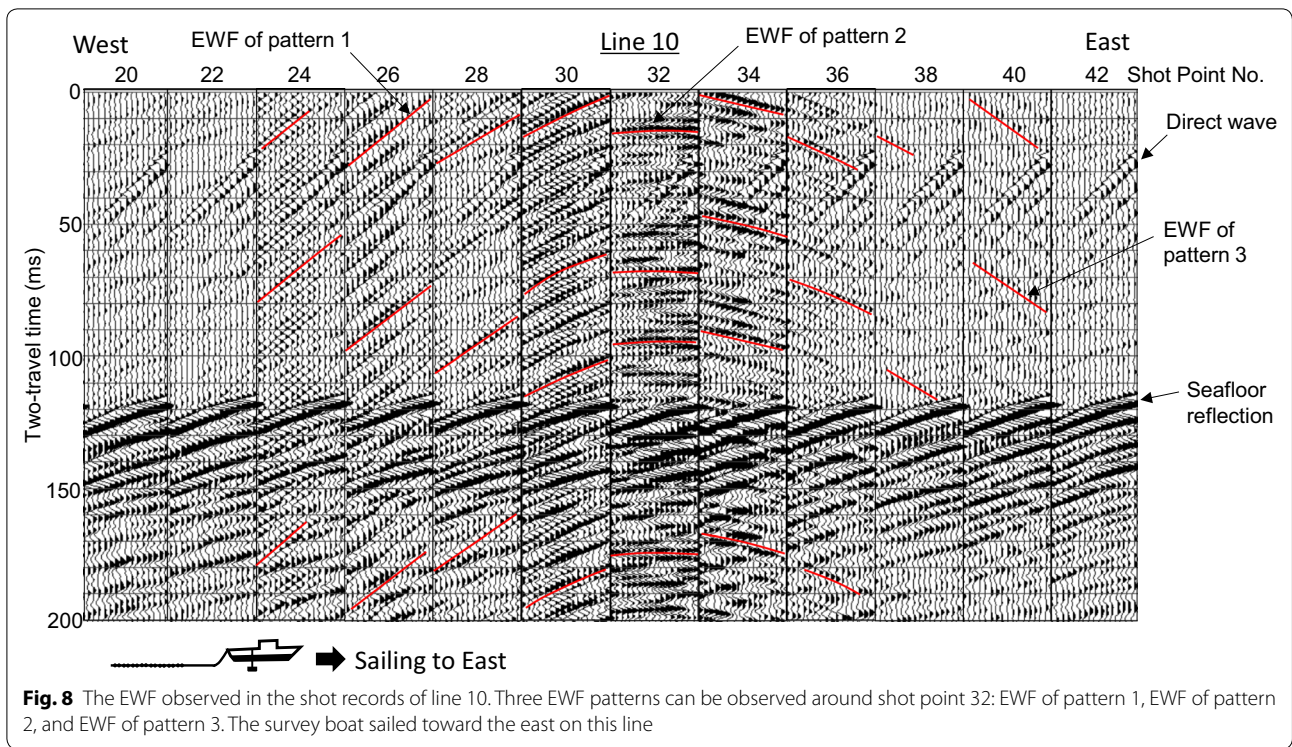
From where did the fluid flow come? It is natural that the fluid would discharge from Fault A and/or C since the most obvious EWF on line 10 appears above the seafloor near Faults C as well as A, as shown in Fig. 13. However, this appearance position of the most obvious EWF is

Table 1 Velocity estimation errors caused by feathering

Feathering

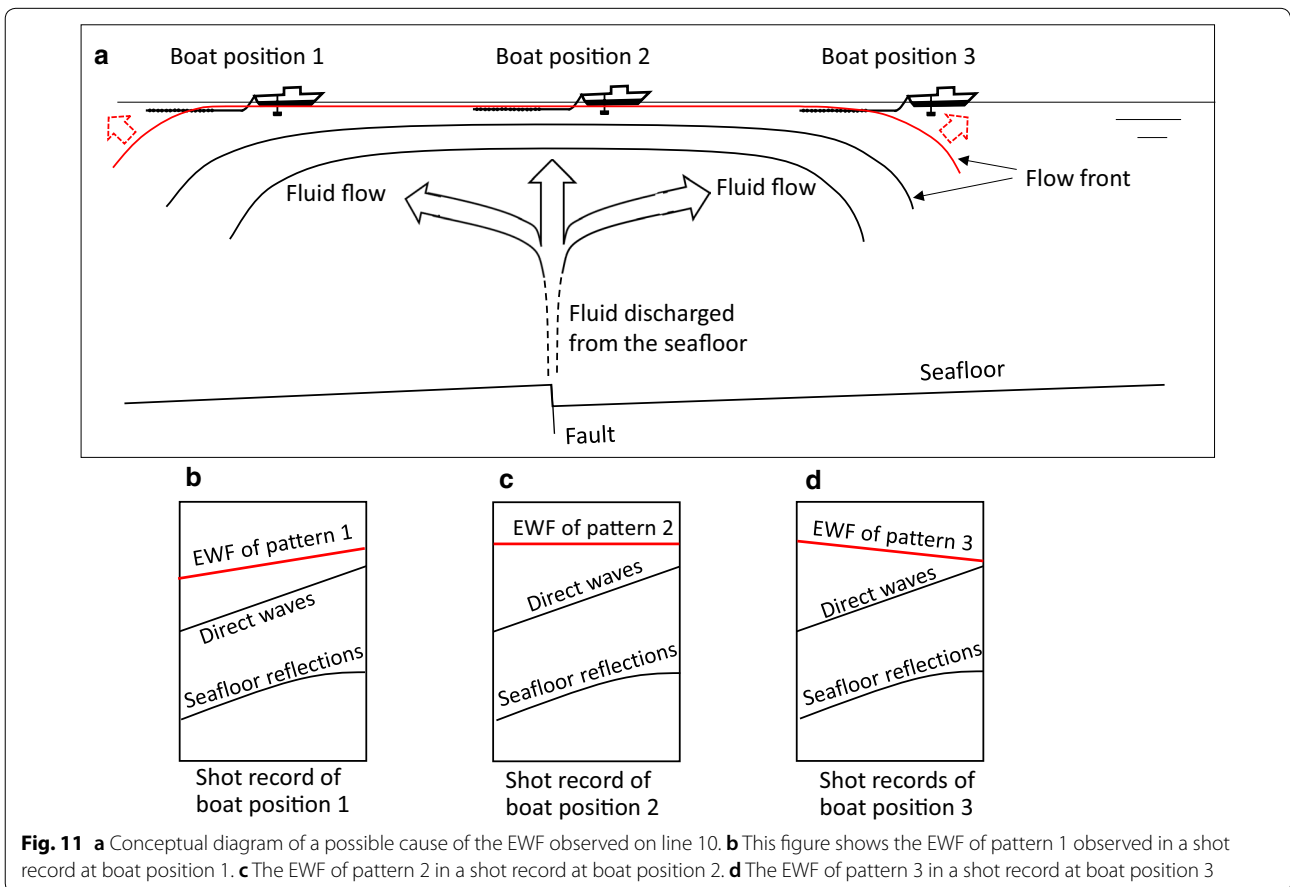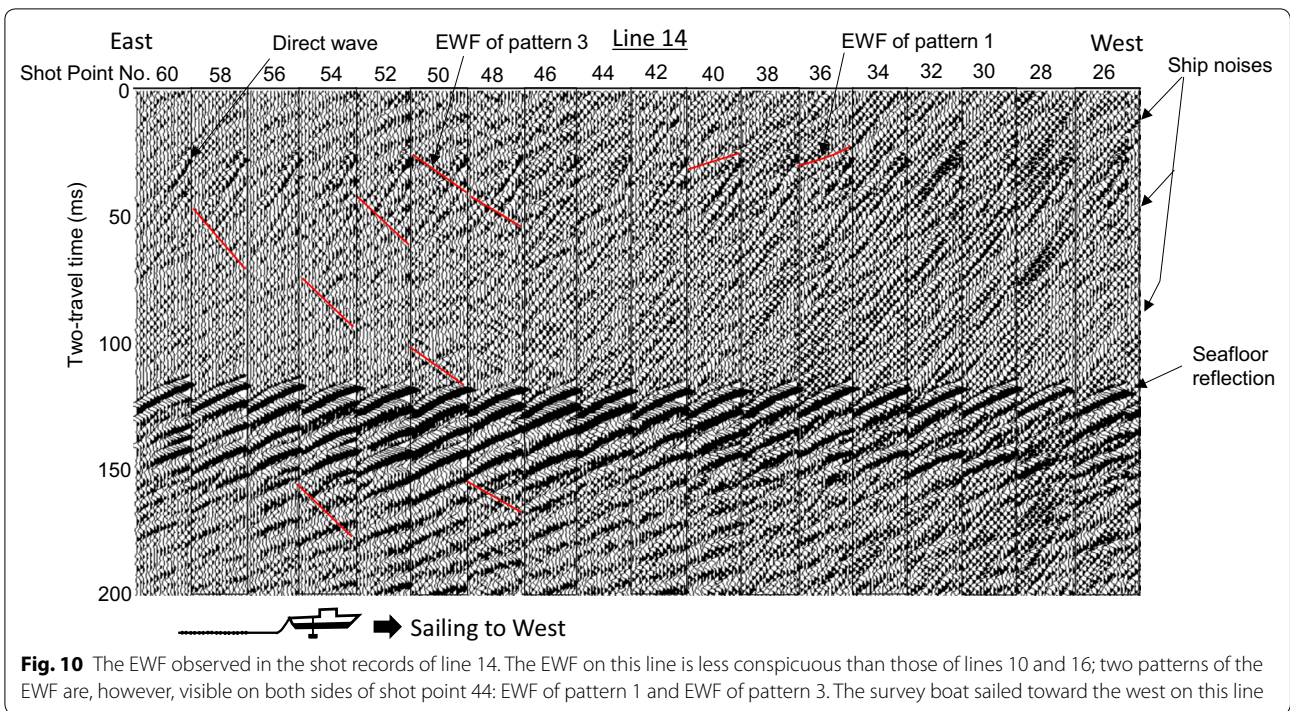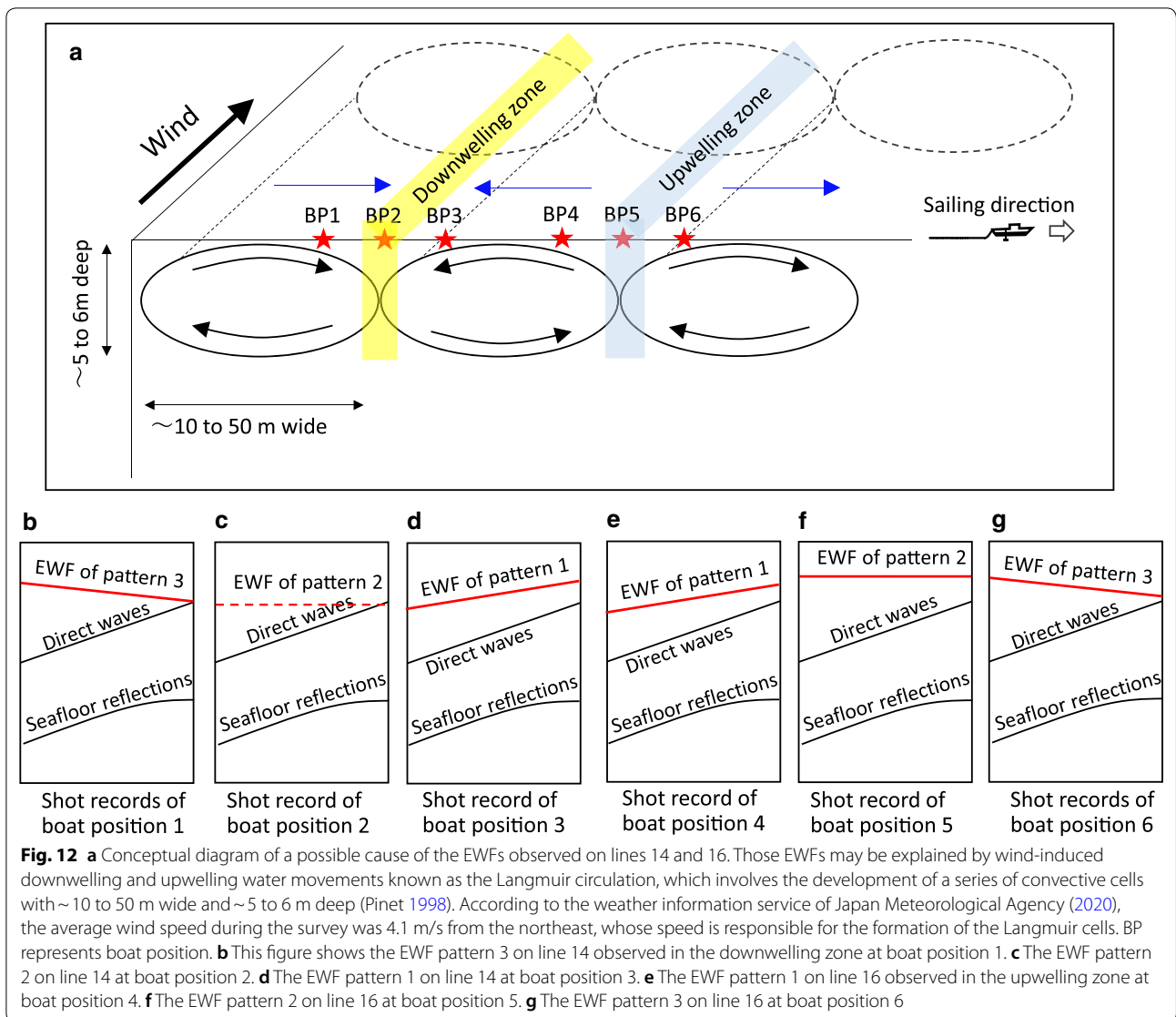| Channel no.	0°	7.5°	15°	22.5°	30°	37.5°	45°	52.5°	60°	67.5°	75°	82.5°	90°
1	1.000	1.000	1.000	1.000	1.000	1.000	1.000	1.000	1.000	1.000	1.000	1.000	1.000
2	1.000	1.000	1.000	1.000	1.000	1.000	1.000	1.000	1.000	1.000	1.000	1.000	1.000
3	1.000	1.000	1.000	1.000	1.000	1.000	1.000	1.000	1.000	1.000	1.000	1.000	1.000
4	1.000	1.000	1.000	1.000	1.000	1.000	1.000	1.000	1.000	1.000	1.000	1.000	1.000
5	1.000	1.000	1.000	1.000	1.000	1.000	1.000	1.000	1.000	1.000	1.000	1.000	1.000
6	1.000	1.000	1.000	1.000	1.000	1.000	1.000	1.000	1.000	1.000	1.000	1.001	1.001
7	1.000	1.000	1.000	1.000	1.000	1.000	1.000	1.000	1.001	1.001	1.001	1.001	1.001
8	1.000	1.000	1.000	1.000	1.000	1.000	1.001	1.001	1.001	1.001	1.001	1.002	1.002
9	1.000	1.000	1.000	1.000	1.000	1.001	1.001	1.001	1.001	1.002	1.002	1.003	1.003
10	1.000	1.000	1.000	1.000	1.001	1.001	1.001	1.002	1.002	1.003	1.003	1.004	1.005
11	1.000	1.000	1.000	1.001	1.001	1.001	1.002	1.002	1.003	1.004	1.005	1.006	1.007
12	1.000	1.000	1.000	1.001	1.001	1.002	1.002	1.003	1.004	1.006	1.007	1.008	1.010
13	1.000	1.000	1.000	1.001	1.001	1.002	1.003	1.005	1.006	1.007	1.009	1.011	1.013
14	1.000	1.000	1.001	1.001	1.002	1.003	1.004	1.006	1.008	1.010	1.012	1.014	1.017
15	1.000	1.000	1.001	1.001	1.003	1.004	1.006	1.008	1.010	1.012	1.015	1.018	1.022
16	1.000	1.000	1.001	1.002	1.003	1.005	1.007	1.010	1.012	1.016	1.019	1.023	1.027
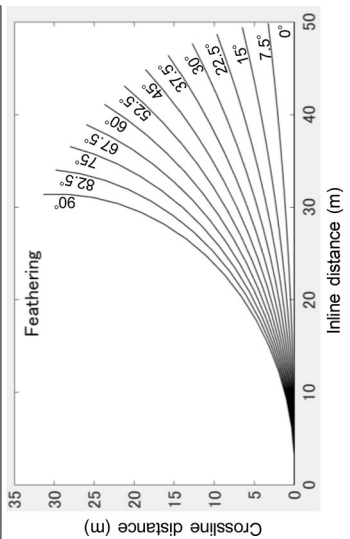
This table shows the result of a simple model for velocity estimation errors caused by feathering. The feathering causes a maximum of up to 2.7% of velocity error

Fig. 8 The EWF observed in the shot records of line 10. Three EWF patterns can be observed around shot point 32: EWF of pattern 1, EWF of pattern 2, and EWF of pattern 3. The survey boat sailed toward the east on this line

Fig. 9 The EWF observed in the shot records of line 16. Three EWF patterns can be observed around shot point 50: EWF of pattern 1, EWF of pattern 2, and EWF of pattern 3. The survey boat sailed toward the west on this line

located near the ends of these faults, where the seafloor displacements of these faults are relatively small or zero. Can fluid discharges occur at the end segments of faults?

According to numerical simulations of strike–slip faults, stress concentration occurs at the end of a fault causing fractures (Kusumoto et al. 2001). Boles et al. (2001)
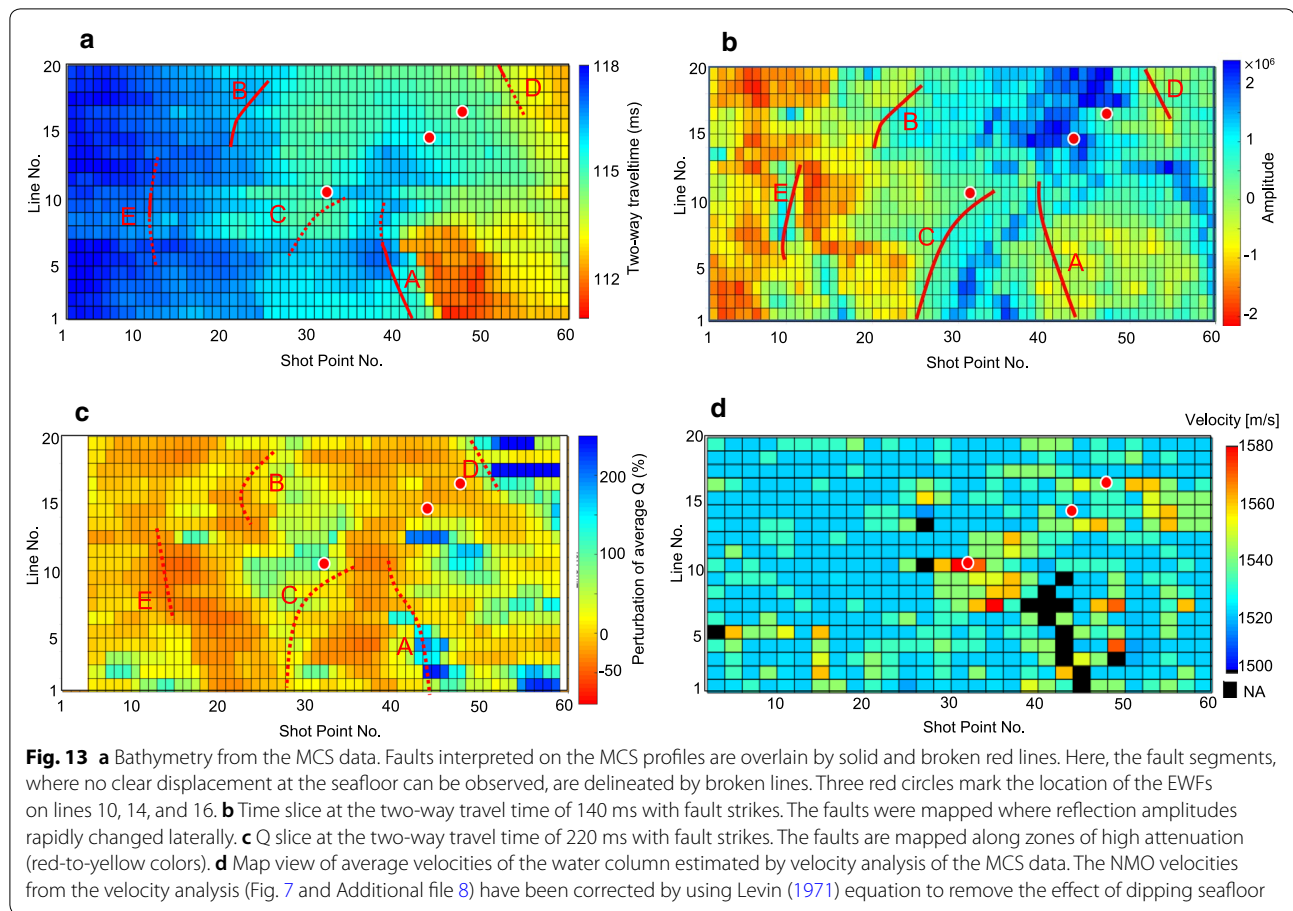
Fig. 10 The EWF observed in the shot records of line 14. The EWF on this line is less conspicuous than those of lines 10 and 16; two patterns of the EWF are, however, visible on both sides of shot point 44: EWF of pattern 1 and EWF of pattern 3. The survey boat sailed toward the west on this line

Fig. 11 **a** Conceptual diagram of a possible cause of the EWF observed on line 10. **b** This figure shows the EWF of pattern 1 observed in a shot record at boat position 1. **c** The EWF of pattern 2 in a shot record at boat position 2. **d** The EWF of pattern 3 in a shot record at boat position 3

Fig. 12 a Conceptual diagram of a possible cause of the EWFs observed on lines 14 and 16. Those EWFs may be explained by wind-induced downwelling and upwelling water movements known as the Langmuir circulation, which involves the development of a series of convective cells with ~ 10 to 50 m wide and ~ 5 to 6 m deep (Pinet 1998). According to the weather information service of Japan Meteorological Agency (2020), the average wind speed during the survey was 4.1 m/s from the northeast, whose speed is responsible for the formation of the Langmuir cells. BP represents boat position. **b** This figure shows the EWF pattern 3 on line 14 observed in the downwelling zone at boat position 1. **c** The EWF pattern 2 on line 14 at boat position 2. **d** The EWF pattern 1 on line 14 at boat position 3. **e** The EWF pattern 1 on line 16 observed in the upwelling zone at boat position 4. **f** The EWF pattern 2 on line 16 at boat position 5. **g** The EWF pattern 3 on line 16 at boat position 6

discovered calcite within a fault shear zone at both end segments of a strike–slip fault (Refugio–Carneros fault in the USA), revealing that fluids migrated through highly fractured zones and precipitated the calcite. From these studies, the fluid might be transported along fractures near the end segments of Faults A and/or C.

Regarding occurrence time of the fluid discharge, it seems to be less than 20 min and more than 6 s. The average observation time for a seismic line is 20 min, including a transit time to the next line, and the most obvious EWF observed on line 10 does not appear on both lines 9 and 11, 20 min before and 20 min after. These two lines

are only 10 m from line 10. This observation suggests that the occurrence time would be less than 20 min. Next, the EWF can be seen throughout the raw field data on shot point 32, which is located at the center of the EWF on line 10. Since the record length of the raw field data is 6 s, the occurrence time would be greater than 6 s. Although estimating the occurrence time of the fluid discharge quantitatively in this study is difficult, the occurrence time would be between 6 s and 20 min. Moreover, from the appearance and non-appearance of the most obvious EWF on the adjacent seismic lines, some fluid discharge

Tsuru *et al. Earth, Planets and Space* (2020) 72:121

Page 14 of 15

Fig. 13 a Bathymetry from the MCS data. Faults interpreted on the MCS profiles are overlain by solid and broken red lines. Here, the fault segments, where no clear displacement at the seafloor can be observed, are delineated by broken lines. Three red circles mark the location of the EWFs on lines 10, 14, and 16. **b** Time slice at the two-way travel time of 140 ms with fault strikes. The faults were mapped where reflection amplitudes rapidly changed laterally. **c** Q slice at the two-way travel time of 220 ms with fault strikes. The faults are mapped along zones of high attenuation (red-to-yellow colors). **d** Map view of average velocities of the water column estimated by velocity analysis of the MCS data. The NMO velocities from the velocity analysis (Fig. 7 and Additional file 8) have been corrected by using Levin (1971) equation to remove the effect of dipping seafloor

might have been occurring intermittently in the survey area, although its occurrence time is unknown.

Conclusions

A high-resolution dense-2D MCS survey was conducted in Uchiura Bay off Numazu, Japan. As a result, active faults cutting the reflections of the seafloor (Faults A and B) and potentially active faults cutting those immediately below the seafloor (Fault C, D, and E) were clearly observed on the MCS profiles. Combining both time and Q slices allowed for more straightforward fault trend interpretation. The most obvious active fault, Fault A, showed the large vertical displacement change at the seafloor, which exceeds 2 m within a short horizontal distance of 50 m.

The EWF was observed within the water column above the seafloor near Fault C. From the three EWF patterns and the results of the velocity analysis, the EWF might be related to some high-temperature fluid flow. The location of the most obvious EWF implies that the fluid rises from a possible fracture zone near the end segments of Faults A and/or C. Considering that no EWF can be seen on lines 9 and 11, which are adjacent to line 10 where the

most obvious EWF was observed, some high-temperature fluids might have been discharging intermittently from the seafloor in the study area.

Supplementary information

Additional file 1. Number of cells interpolated or decimated for regularization of 3D seismic cube. In lines 1–5, 10–17 % of empty cells were interpolated. There are no empty cells interpolated in the other lines, because of improved skill in low-speed (2 kn) boat control during the survey.

Additional file 2. Method of seismic attenuation profiling (SAP).

Additional file 3. Seismic profiles of all MCS lines.

Additional file 4. Time slices of 120 to 220 ms in two-way traveltimes.

Additional file 5. Q slices of 120 to 220 ms in two-way traveltimes.

Additional file 6. Raw data, rms amplitude, shot record and velocity.

Additional file 7. Seawater velocity modeling by using the equation of Mackenzie (1981). The calculated velocity was plotted for temperature from 10 to 70 °C as a function of salinity ranging from 32 to 38 ‰, in case of water depth of 50 m. This equation is applicable below 30 °C. Light yellow hatch indicates a temperature zone extrapolated by this relational expression.

Additional file 8. Results of velocity analysis.

Tsuru *et al. Earth, Planets and Space*   (2020) 72:121

Page 15 of 15

Author details

[1] Department of Marine Resources and Energy, Tokyo University of Marine Science and Technology, 4-5-7 Konan, Minato-ku, Tokyo 108-8477, Japan. [2] Atmosphere and Ocean Research Institute, The University of Tokyo, 5-1-5, Kashiwanoha, Kashiwa-shi, Chiba 277-8564, Japan. [3] Research Institute for Marine Geodynamics, Japan Agency for Marine-Earth Science and Technology, Yokohama 236-0001, Japan. [4] Geological Survey of Japan, National Institute of Advanced Industrial Science and Technology, 1-1-1 Higashi, Tsukuba, Ibaraki 305-8567, Japan.

References

Boles J, Clark J, Leifer I, Washburn L (2001) Temporal variation in natural methane seep rate due to tides, Coal Oil Point area, California. J Geophys Res 106:27077–27086

Chen JX, Song HB, Guan Y-X, Yang S-X, Bai Y, Geng MH (2017) A preliminary study of submarine cold seeps by seismic oceanography techniques. Chin J Geophys 60:117–129

Gray M, Bell R, Morgan J, Henrys S, Barker D, IODP Expedition 372 scientists, IODP Expedition 375 scientists et al (2019) Imaging the shallow subsurface structure of the north Hikurangi subduction zone, New Zealand, using 2D full-waveform inversion, J. Geophys. Res. Solid Earth 124:9049–9074

Japan Meteorological Agency (2020) Weather information service of Japan Meteorological Agency. https://www.data.jma.go.jp/obd/stats/etrn/. Accessed 13 June 2020

Kusumoto S, Fukuda Y, Takemura K, Takemoto S (2001) Forming mechanism of the sedimentary basin at the termination of the right-lateral left-stepping faults and tectonics around Osaka Bay. J Geogr 110:32–43

Kutsuwada K, Tanikawa M, Hagiwara Y, Katsumata T (2007) Long-term variability of upper oceanic condition in Suruga Bay and its surrounding area. Oceanogr Jpn 16:277–290 **(in Japanese with English abstract)**

Langmuir I (1938) Surface motion of water induced by a wind. Science 87:119–123

Levin F (1971) Apparent velocity from dipping interface reflections? Geophysics 36(3):510–516

Mackenzie K (1981) Nine-term equation for the sound speed in the oceans. J Acoust Soc Am 70:807–812

Matsumoto M, Nishimura T (1998) Mersenne twister: a 623-dimensionally equidistributed uniform pseudo-random number generator. ACM Trans Model Comput Simul 8(1):3–30

Misawa Y (1990) Suruga Bay, Japan, Marine Geology. Tokai University Press, Tokyo

Nagumo, S. (2000) Pre-Stack Profiling Method, The 103rd annual meeting of Society of Exploration Geophysicists of Japan, Proceedings, 103, 20–24 **(in Japanese with English abstract)**

Nishimura S, Nishida J, Nogi T (1986) Gravity and magnetotelluric interpretation of the southern part of the Fossa Magna region, Central Japan. J Phys Earth 34:171–185

ODP Leg 110 Scientific Party (1987) Expulsion of fluids from depth along a subduction-zone decollement horizon. Nature 326:785–788

Park J, Tsuru T, Kodaira S, Cummins PR, Kaneda Y (2002) Splay fault branching along the Nankai subduction zone. Science 297(5584):1157–1160

Pinet PR (1998) Invitation to oceanography. Jones & Bartlett Publishers, Sudbury

Sano Y, Hara T, Takahata N, Kawagucci S, Honda M, Nishio Y, Tanikawa W, Hasegawa A, Hattori K (2014) Helium anomalies suggest a fluid pathway from mantle to trench during the 2011 Tohoku-Oki earthquake. Nat Commun 5:3084. https://doi.org/10.1038/ncomms4084

Sato T (2014) Preliminary results of the seismic reflection survey in the coastal sea area of Suruga Bay. Jpn, Geol Surv Jpn Interim Report 65:1–11 **(in Japanese with English abstract)**

Shipley T, Moore G, Bangs N, Moore C, Stoffa P (1994) Seismically inferred dilatancy distribution, northern Barbados Ridge decollement: implications for fluid migration and fault strength. Geology 22:411–414

The Tanna Fault trenching research group (1983) Trenching study for Tanna Fault, Izu, at Myoga, Shizuoka Prefecture, Japan. Bull Earthq Res Inst 58:797–830 **(in Japanese with English abstract)**

Tsuji T, Kawamura K, Kanamatsu T, Kasaya T, Fujikura K, Ito Y, Tsuru T, Kinoshit M (2013) Extension of continental crust by anelastic deformation during the 2011 Tohoku-oki earthquake: the role of extensional faulting in the generation of a great tsunami, Earth Planet. Sci. Lett. 364:44–58

Tsuneishi Y, Shiosaka K (1981) Fujikawa Fault and Tokai Earthquake. J Jpn Soc Eng Geol 22:52–66 **(in Japanese with English abstract)**

Tsuru T, No T, Fujie G (2017) Geophysical imaging of subsurface structures in volcanic area by seismic attenuation profiling. Earth Planets Space 69:5. https://doi.org/10.1186/s40623-016-0592-0

Tsuru T, Park J-O, No T, Kido Y, Nakahigashi K (2018) Visualization of attenuation structure and faults in incoming oceanic crust of the Nankai Trough using seismic attenuation profiling. Earth Planets Space 70:31. https://doi.org/10.1186/s40623-018-0803-y

Tsuru T, Amakasu K, Park J-O, Sakakibara J, Takanashi M (2019) A new seismic survey technology using underwater speaker detected a low-velocity zone near the seafloor: an implication of methane gas accumulation in Tokyo Bay. Earth Planets Space 71:31. https://doi.org/10.1186/s40623-018-0803-y

Yilmaz O, Doherty S (1987) Seismic data processing, vol 2. SEG, Tulsa

Publisher's Note

Springer Nature remains neutral with regard to jurisdictional claims in published maps and institutional affiliations.